Classification of Hyperspectral Image by CNN Based on Shadow Area Enhancement Through Dynamic Stochastic Resonance

XUEFENG LIU[1], HAO WANG[1], YUE MENG[1], AND MIN FU[2]
[1]College of Automation and Electronic Engineering, Qingdao University of Science and Technology, Qingdao, China
[2]College of Information Science and Engineering, Ocean University of China, Qingdao, China

Corresponding author: Min Fu (fumin@ouc.edu.cn)

ABSTRACT Target detection and classification in the shadow area of hyperspectral images (HSIs) has always been an important problem in the field of HSI data processing. However, there are few methods to detect or classify targets in the shadow area effectively because of occlusion of objects or oblique solar radiation. Dynamic stochastic resonance (DSR) theory shows that under the synergistic action of weak input signal, noise and non-linear system, the energy of noise can be transferred into signal partially. It breaks the idea that signal can be enhanced only by eliminating noise and has been proved to be effective in many fields. In this paper, DSR is introduced into the shadow area enhancement of HSI from both spatial and spectral dimensions. Then, the enhanced HSI data can be obtained by fusing the processed shadow with the original HSI data. Finally, 2D convolutional neural networks (2D-CNN) is used to classify the enhanced HSI. To evaluate the proposed method, a real-world HSI has been processed in the experiment and the results show that DSR can improve the contrast and the spectral intensity of HSI shadow area. Compared to other state-of-the-art methods, the classification accuracy is better at containing different targets with small samples, especially in the spectral dimension.

INDEX TERMS Convolutional neural network, remote sensing images, shadow region, stochastic resonance, DSR parameter optimization.

I. INTRODUCTION

Based on the theory of electromagnetic wave, hyperspectral remote sensing technology provides abundant information of ground objects by accurately receiving and recording the complex interactions between electromagnetic wave and objects [1], so hyperspectral images (HSIs) containing both spatial and spectral information of objects can help to improve the classification and target detection [2]. HSIs have been widely used in earth observation [3], military, environmental monitoring [4] and precision agriculture fields [5] etc.

Because of the linear propagation and impermeability of light, the HSIs under the condition of occlusion of objects or oblique solar radiation would contain shadow areas [6]. But, not only the contrast and brightness in the shadow areas of HSIs are relatively low [7], but also the spectral lines of the pixels are weak [8] and the samples in the shadow areas are

The associate editor coordinating the review of this manuscript and approving it for publication was Wenming Cao.

generally small. Those situations pose a great challenge to the information exploration of the shadow area in HSIs. Due to lack of effective methods, the possible targets and valuable information in shadow areas would be lost.

As an important way to explore the rich information in HSIs, the classification of HSIs is to discriminate each pixel in the image with abundant spatial and spectral data [9]. Besides some classic classification methods, support vector machine (SVM) [10], spectral angle mapping (SAM) [11] and clustering [12] etc., also some state-of-the-art methods have been introduced to HSI classification, such as, deep belief network (DBN) [13], convolutional neural networks (CNN) [14] [15] and so on. By extracting the spatial or the spectral features, most of these methods have presented the capability in HSI classification, but could not help to classify the targets in the shadow areas due to low brightness and contrast.

In image processing, there are some image enhancement methods. For example, dark-channel prior (DCP) [16] and

Retinex algorithm [17] are designed mainly for gray and RGB image, and dynamic stochastic resonance (DSR) [18] derived from the stochastic resonance (SR) theory which was developed to explain the Quaternary glacier problem [18] has been proven the prospective in weak signal processing and dark image enhancement [19].

In this paper, a method combined shadow enhancement and classification is proposed. Firstly, the DSR technology is introduced into the shadow enhancement of HSI from the perspective of space and spectrum and the enhanced shadow areas in the format of 2-dimension (2D) data could be obtained. Then, the enhanced areas could be fused with the original image. Finally, the processed HSI could be classified by 2D convolutional neural networks (2D-CNN) due to its promising classification performance and its structural consistence with the HSI data.

The remainder of this paper is organized as follows: Section II overviews the main theory of DSR and 2D-CNN; the proposed method is presented in Section III on details; Section IV presents the experimental results and discussion; the conclusion is contained in Section V.

II. OVERVIEW OF ALGORITHMS
A. DYNAMIC STOCHASTIC RESONANCE
In signal processing, noise generally decreases signal-to-noise ratio and suppresses the information extraction. But, in some specific nonlinear systems, the existence of noise can enhance weak signal. A SR system can be expressed as [20]:

$$m\frac{d^2x(t)}{dt} + \gamma\frac{dx(t)}{dt} = -\frac{dU(x)}{dx} + f(t) + \xi(t) \quad (1)$$

where t stands for time, m and γ represent the mass and friction coefficients of moving particles, $\xi(t)$ and $f(t)$ are the noise effects and periodic driving forces of particles moving in a bistable potential well respectively, $x(t)$ means the position of the particle and $\frac{dx(t)}{dt}$ is the rate of change. (1) describes the motion of over-damped particles in a bistable potential well, which determined by $U(x)$ as bellow [19]:

$$U(x) = -a\frac{x^2}{2} + b\frac{x^4}{4} \quad (2)$$

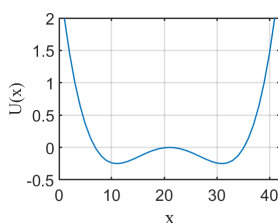where a and b are parameters of the system. Fig. 1 illustrates the system situation when $a = 1$ and $b = 1$.

FIGURE 1. Bistable potential system ($a = 1, b = 1$).

If the model is seriously over-damped, the equation can be simplified as [21]:

$$\frac{dx(t)}{dt} = -\frac{dU(x)}{dx} + f(t) + \xi(t) \quad (3)$$

Bring (2) into (3), then:

$$\frac{dx(t)}{dt} = ax(t) - bx(t)^3 + f(t) + \xi(t) \quad (4)$$

Equation (4) has two stable points $x_\pm = \pm\sqrt{\frac{a}{b}}$, and a barrier $\triangle U = \frac{a^2}{4b}$ in the middle. If the periodic driving force is absent, the system will remain stable. As shown in Fig. 2, when the periodic driving force acts on the bistable system, the stable state will be destroyed and the potential well will change periodically with the action of external periodic driving. When the external periodic driving force and noise act together on the bistable system, the noise will give the particles the energy to transit from one stable state to another. That means, the noise energy can be used to improve the strength of weak signal in a SR system.
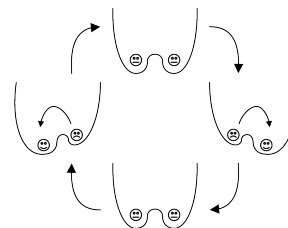

FIGURE 2. The change of potential well under the influence of periodic signal.

So, if the shadow areas in HSIs are regarded as weak signals disturbed by noise, they can be enhanced by a DSR system. When it is applied to enhance the shadow areas, the DSR system described in (4) should be transformed into a differential form [22]:

$$x(n + 1) = x(n) + \triangle t[(ax(n) - bx^3(n)) + Input] \quad (5)$$

where n is the number of iterations, $x(n + 1)$ is the output of DSR, $\triangle t$ is the step size. *Input* refers to hyperspectral data with shadow areas: $Input = f(t) + \xi(t)$.

B. 2D CONVOLUTIONAL NEURAL NETWORK
As a representation of deep learning, CNN avoids the drawbacks of artificial feature extraction and reduces the network parameters with sharing weights [23]. It has demonstrated the impressive ability of feature extraction [24]. The consistency of 2D-CNN and HSI data structure makes the method a convenient solution for HSI classification.

2D-CNN framework is composed of input layer, convolution layers, pooling layers and full connection layers as shown in Fig. 3.

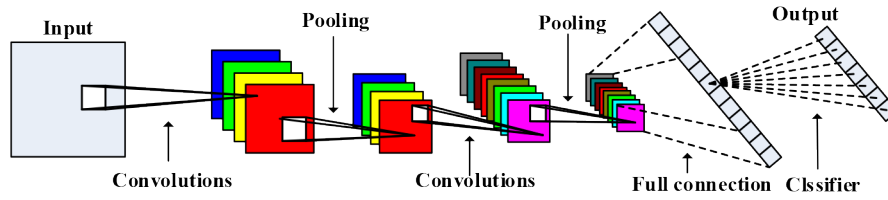The input layer is the 1st, and the input data should be a 2D tensor.

FIGURE 3. 2D-CNN framework.

The core part of CNN is the convolution layer in which the convolution operations are generally used to extract features and introduce some non-linear factors to the network through activation functions. The value of a neuron at position (x, y) of the m feature map in the l layer can be given by [25]:

$$v_{xy}^{lm} = f\left(\sum_{p} \sum_{n_1=0}^{N_1-1} \sum_{n_2=0}^{N_2-1} \omega_{lmp}^{n_1 n_2} v_{(l-1)p}^{(x+n_1)(y+n_2)} + b_{lm}\right) \quad (6)$$

where p indexes the feature map in the $(l-1)$th layer connected to the current mth feature map, $\omega_{lmp}^{n_1 n_2}$ is the weight of position (n_1, n_2), $n_1 = 0, \ldots, N_1 - 1$ and $n_2 = 0, \ldots, N_2 - 1$ connected to the pth feature map, N_1 and N_2 are the height and the width of the convolution kernel, and b_{lm} is the bias of the m feature map in the l layer. f is the activation function and the common options are rectified linear units (ReLU), Sigmoid and Tanh [26] etc.

The pooling layers can subsample the feature maps and reduce the number of network parameters [27].

The full connection layer can convert the input matrix into a 1D vector.

At the end of network, a softmax regression can be set as a classifier to convert the network output into a probability distribution [28]:

$$OUT = softmax(O_\varphi) = \frac{e^{O_\varphi}}{\sum_{\varphi=1}^{\Phi} e^{O_\varphi}} \quad (7)$$

where OUT with a value between 0 and 1 is the output after the softmax classifier, φ is the actual output class of the sample after passing through the network, $O_\varphi(\varphi = 1, 2, \ldots, \Phi)$ is the ordinal number of class and Φ means the total class number of the target data.

III. HSI CLASSIFICATION BASED ON DSR SHADOW ENHANCEMENT AND 2D-CNN

To explore and detect the possible targets in the shadow areas in HSIs, an improved classification method combined DSR shadow enhancement and 2D-CNN is proposed in this paper and the main procedure is shown in Fig. 4.

As a three-dimension (3D) tensor, hyperspectral data can be expressed as: $\mathbb{R}^{H \times W \times B}$, where $\mathbb{R}$ presents a HSI tensor, H is the width, W is the height, and B is the number of spectral bands, respectively. The spectral vector at spatial location (i, j) can be defined as $X_{i,j} = [x_{i,j,1}, \ldots, x_{i,j,B}] \in \mathbb{R}$, where $x_{i,j,1}, \ldots, x_{i,j,B}$ represent the spectral intensity of B bands at
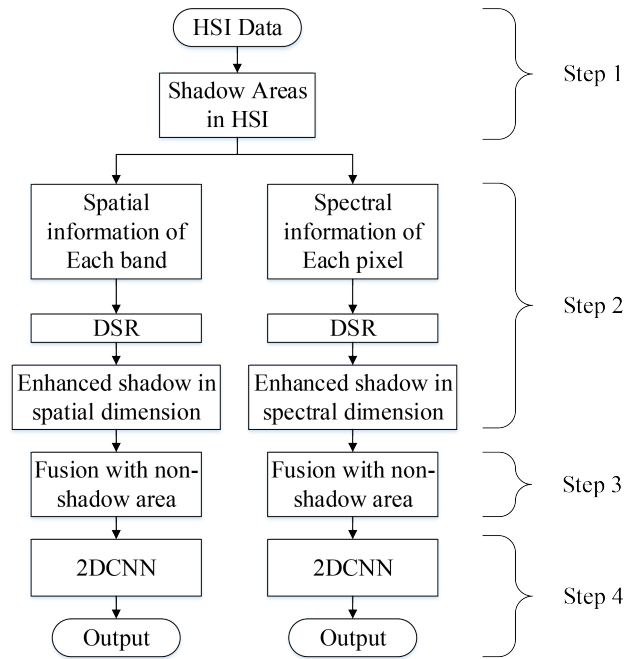

FIGURE 4. The main procedure of the proposed method.

position (i, j). The 2D spatial data can be defined as $Y_k \in \mathbb{R}$, where k represents the number of band of hyperspectral data with $k = 1, \ldots, B$, and Y_k is a matrix with the size of $H \times W$. The specific steps of the proposed method are detailed as follows:

Step 1: A shadow extraction mask made from the ground truth image is used to extract the shadow area in HSI, so that only shadow area will be further processed. After mask extraction, a 3D HSI shadow data $\mathbb{R}^s$ could be obtained from the original HSI data $\mathbb{R}$.

Step 2: Because the hyperspectral data has both spatial and spectral characteristics, the 3D shadow areas extracted from the HSI could be enhanced from two perspectives of spatial and spectral dimensions.

- DSR on the spatial dimension: For each band, there is a 2D spatial data $Y_k^s \in \mathbb{R}^s$, $k = 1, \ldots, B$. Because only 1D sequence can be calculated by (5), 2D data must be reshaped into a 1D sequence before DSR enhancement. For the next step, the 1D vector should be transformed back into 2D matrix.

- DSR on the spectral dimension: For each pixel, the spectral vector $X_{i,j}^s = [x_{i,j,1}^s, \ldots, x_{i,j,B}^s] \in \mathbb{R}^s$ could be extracted and processed by DSR in (5).
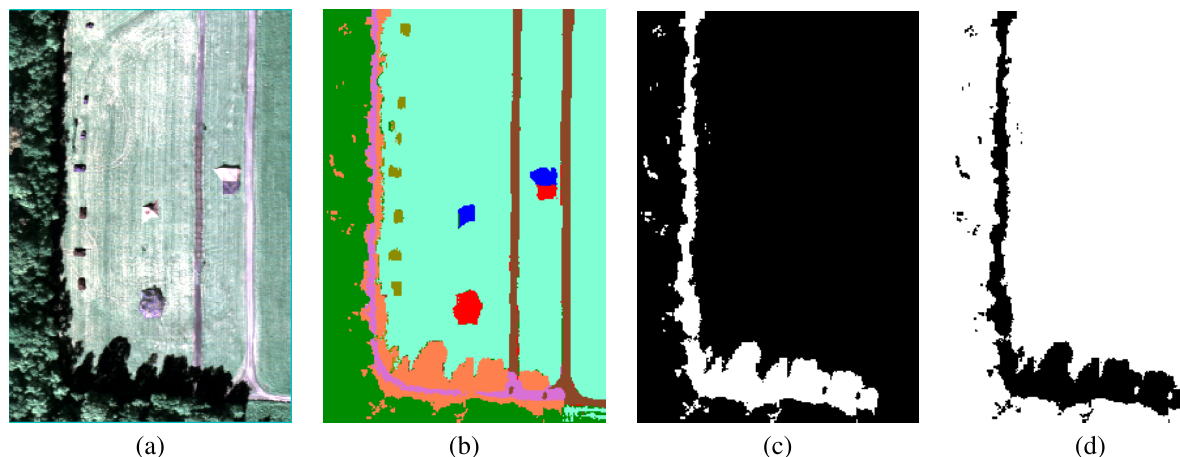
FIGURE 5. (a) HYDICE HSI data. (b) Ground truth of HYDICE HSI. (c) Shadow extraction mask. (d) Shadow fusion mask.

TABLE 1. Land-cover classes and number of samples of ROI1 in the HYDICE HSI.

No	Color	Classes	Number of pixels
1		Grass	41480
2		Tree	13562
3		Road	4220
4		Road under Shadow	2108
5		Shadow	5169
6		Target1	671
7		Target2	404
8		Target3	642
All Classes			68256

Step 3: A fusion mask contrary to the shadow extraction mask is used to fuse the enhanced shadow data with the original HSI, so that the HSIs with enhanced shadow areas could be acquired in spatial and spectral dimensions respectively.

Step 4: The fused images are 2D data, therefore, 2D-CNN can be used to classify the enhanced HSI.

IV. EXPERIMENT

A real-world HYDICE (Hyperspectral Digital Imagery Collection Experiment) HSI data is processed to evaluate the performance of the proposed method. This HYDICE HSI shown in Fig. 5(a) has a 0.75 m spatial and 10nm spectral resolution and includes 148 spectral bands (from 435 to 2326 nm), 316 rows and 216 columns. It can be denoted by $X \in \mathbb{R}^{316 \times 216 \times 148}$ and there are 7 land cover classes: field, trees, road, shadow (including a section of road) and three different targets as shown in Fig. 5(b) and Table 1.

As mentioned in **Step 1** and **3** in Section III, the shadow extraction mask of the HYDICE HSI and the shadow fusion mask are illustrated in Fig. 5(c) and Fig. 5(d). In order to verify the enhancement effect of DSR, two groups of regions of interest (ROI) are selected for comparison. ROI1 contains 8 samples: road, road under shadow, grass, tree, shadow, target 1, target 2, target 3. ROI2 contains 7 samples: road, grass, tree, shadow, target 1, target 2 and target 3. So, there is an additional "road under shadow" in ROI1 compared to

ROI2 where "road" and "road under shadow" are grouped together.

A. SHADOW AREA ENHANCED BY DSR

Because the parameters *a* and *b* in (2) of DSR can determine the position of stable points and height of barrier, they have great influence on the resonance state and should be carefully optimized.

1) DSR PARAMETER OPTIMIZATION

Since there is less discussion on DSR parameter selection, the values of the parameter *a* and *b* of DSR will be traversed in this paper. In the simulation, *a* and *b* can change in a certain range of values and then Pearson correlation coefficients between the enhanced spectral lines and the original ones under different values of *a* and *b* are calculated as a representation of the enhancement effect. The closer to 1 the coefficient is, the stronger the correlation is and the better the DSR enhancement effect will be. Pearson correlation coefficients can be defined as [29]:

$$r = \frac{\sum_{i=1}^{n}(X_i - \overline{X})(Y_i - \overline{Y})}{\sqrt{\sum_{i=1}^{n}(X_i - \overline{X})^2}\sqrt{\sum_{i=1}^{n}(Y_i - \overline{Y})^2}} \tag{8}$$

where *X* and *Y* are two 1D sequences with length of *n*, X_i and Y_i are the *i*th numbers in sequence *X* and *Y*, $\overline{X}$ and $\overline{Y}$ are averages of *X* and *Y* respectively.

The Pearson correlation coefficient with *a* and *b* between 0 and 20 is shown in Fig. 6, which reaches 0.6765 when $a = 0.01$ and $b = 0.01$. Therefore, in the experiment, when DSR is used to enhance the spectral dimension, we set $a = 0.01$, $b = 0.01$.

2) DSR SHADOW ENHANCEMENT

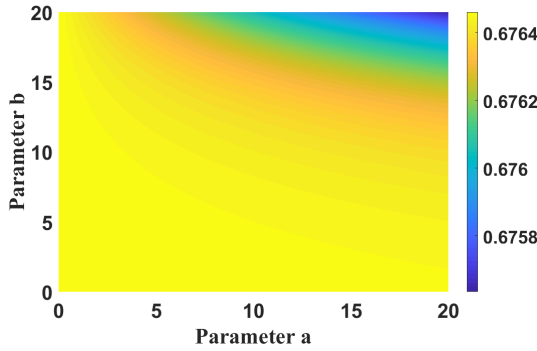According to Step 2 described in Section III, DSR with optimized parameters could be used to enhance the shadow

FIGURE 6. The influence of the parameter *a* and *b* on Pearson correlation coefficient.

areas in the HYDICE HSI. The enhancement results in the spatial dimension are shown in Fig. 7 where the brightness and the contrast of the shadow area in the first band after DSR enhancement have been improved obviously and many details such as the road hidden in the shadow area could be distinguished after DSR processing.
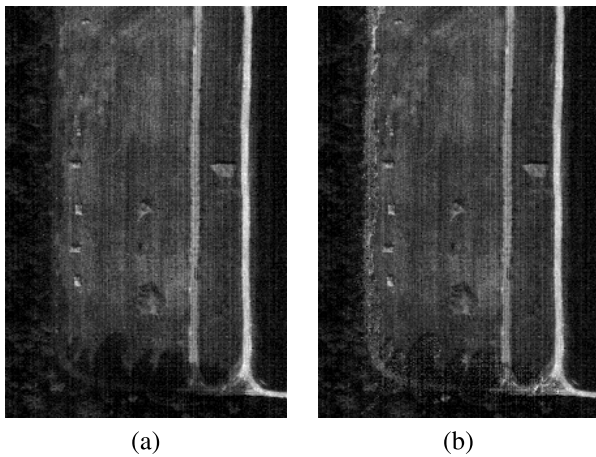

(a)   (b)

FIGURE 7. 1st band of HYDICE HSI before and after DSR Enhancement in the spatial dimension. (a)Before DSR Enhancement. (b)After DSR Enhancement.

The comparison of the spectral information before and after DSR enhancement is plotted in Fig. 8. It can be seen that the characteristics of the spectral information in the shadow area after DSR are more distinct than those before DSR and the reflection of spectrum is enlarged too.

B. 2D-CNN CLASSIFICATION

As preparation, the principal component analysis (PCA) [30] method is used to reduce the dimension of the enhanced HYDICE HSI and provide the input data for 2D-CNN.

After DSR enhancement, 2D-CNN can be used to classify the data. The network structure and related parameters of 2D-CNN used in the experiment are shown in Table 2, where Ci, $(i = 1, 2, 3)$ means the i convolution layer, Pi, $(i = 1, 2)$ is the i polling layer and F represents the full connection layer. In the experiment, ReLU function [26], which can avoid
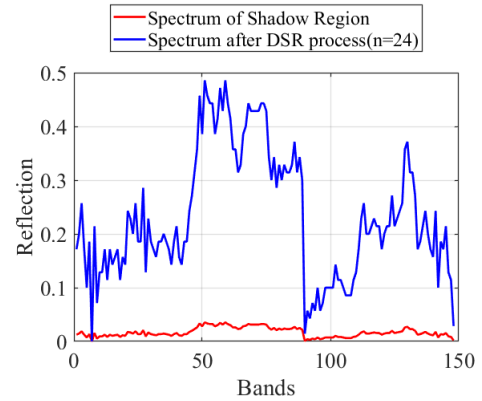

FIGURE 8. The spectral information in the shadow area before and after DSR enhancement.

TABLE 2. 2D-CNN architecture.

Layer	Kernel Size	Kernel Number	Active Function	Dropout
$C1$	4×4	16	ReLU	—
$P1$	2×2	—	—	0.4
$C2$	4×4	32	ReLU	—
$P2$	2×2	—	—	0.4
$C3$	4×4	64	ReLU	—
F	128	—	softmax	0.1

vanishing gradients or exploding gradient problems, has been chosen as the activation function , and max-pooling [27] is used to retain the texture information of images.

In order to obtain as much spatial information as possible, a 27×27 size spatial region around each sample pixel is selected as the input sample.

To evaluate the classification performance quantitatively, overall accuracy (OA) is used [31]:

$$OA = \frac{1}{\lambda} \sum_{r=1}^{R} a_{rr} \qquad (9)$$

where λ is the total number of samples, and a_{rr} is the number of test samples which actually belong to class S_r ($r = 1, 2, \ldots, R$, where R is the total number of classes in the HSI), and also include into S_r by classification.

The parameter of 2D-CNN would be adjusted according to the single variable principle to obtain superior classification performance [32].

C. COMPARISON WITH OTHER CONSIDERED METHODS

In this paper, the well-known DCP image enhancement method is used to compare with DSR method and three widely used methods SAM, SVM and DBN are selected to compare with 2D-CNN. After DCP and DSR enhancement, the considered HSI classification methods would be used to classify the data.

In classification, 10%, 15% and 20% data are selected as training data respectively, and the rest as testing data. The OA values of different methods are listed in Table 3, and the classification results are shown from Fig. 9 to 12.

TABLE 3. Accuracy of classification.

Method	Training Data Percentage	Original HSI		Enhanced HSI by DCP		Enhanced HSI by DSR on Spatial Dimension		Enhanced HSI by DSR on Spectral Dimension	
		ROI1	ROI2	ROI1	ROI2	ROI1	ROI2	ROI1	ROI2
SAM	10%	83.7846%	82.8850%	38.7793%	34.6732%	84.2900%	83.2484%	83.6425%	83.0594%
	15%	83.9780%	82.9275%	38.7936%	34.7153%	84.4483%	83.4549%	83.8402%	83.1824%
	20%	83.9589%	83.0945%	38.8528%	34.8687%	84.4483%	83.6381%	83.7919%	83.2938%
SVM	10%	89.3782%	89.5745%	75.5281%	81.3423%	89.5247%	89.5526%	90.6235%	91.2696%
	15%	89.4222%	89.6624%	75.7631%	81.3751%	89.5115%	89.7108%	91.9040%	92.0080%
	20%	90.1576%	90.4023%	75.7677%	81.3636%	90.1679%	90.4393%	92.0124%	92.1575%
DBN	10%	88.3862%	90.2415%	93.0586%	93.3550%	90.8354%	92.5711%	90.4758%	92.6931%
	15%	91.8121%	91.6056%	94.7035%	95.0134%	94.1211%	94.0503%	93.9215%	93.5304%
	20%	94.5703%	94.2101%	94.8004%	95.0256%	95.3089%	95.2897%	95.2988%	95.5641%
2D-CNN	10%	*95.2456%*	95.1129%	94.8128%	94.8571%	*96.0381%*	95.9214%	*96.1123%*	95.7501%
	15%	95.9511%	95.7931%	95.9375%	95.4526%	96.0924%	95.9745%	96.1453%	*96.2701%*
	20%	95.2805%	95.6031%	95.9567%	94.4601%	95.9787%	96.1099%	96.2486%	*96.5468%*

(a) (b) (c) (d) (e) (f) (g) (h)
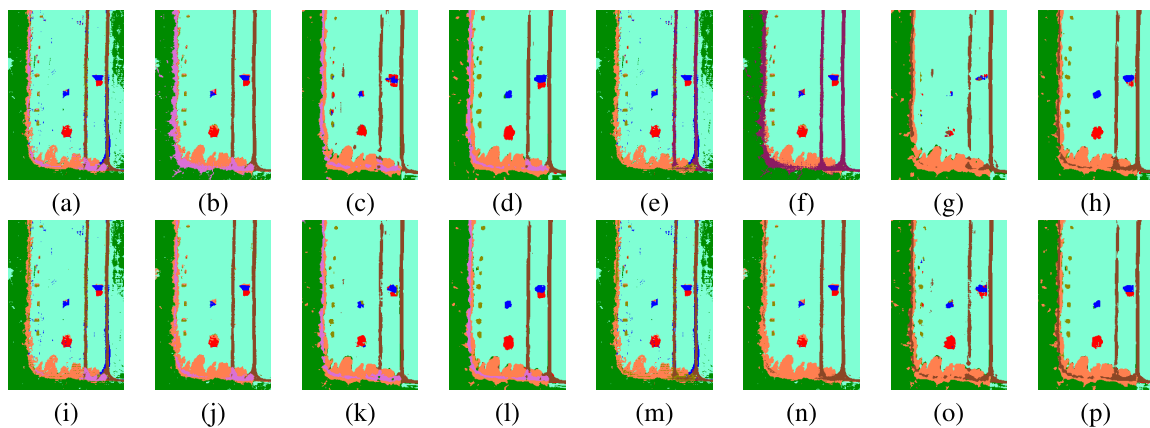
(i) (j) (k) (l) (m) (n) (o) (p)

FIGURE 9. Classification Results of the Original HSI. The (a), (b), (c) and (d) are the classification results of ROI1 using SAM, SVM, DBN and CNN with 10% training data respectively. The (e), (f), (g) and (h) are the classification results of ROI2 using SAM, SVM, DBN CNN with 10% training data respectively. The (i), (j), (k) and (l) are the classification results of ROI1 using SAM, SVM, DBN and CNN with 20% training data respectively. The (m), (n), (o) and (p) are the classification results of ROI2 using SAM, SVM, DBN and CNN with 20% training data respectively.
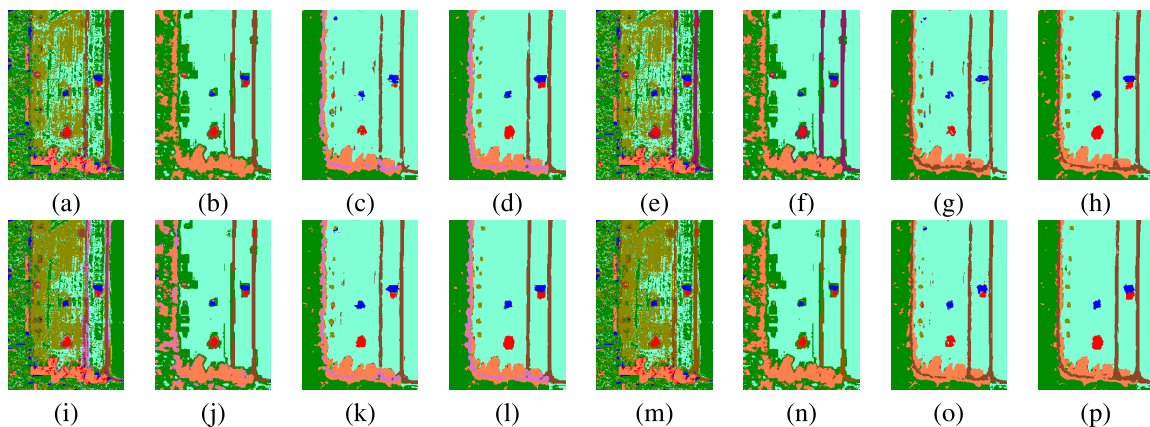

(a) (b) (c) (d) (e) (f) (g) (h)

(i) (j) (k) (l) (m) (n) (o) (p)

FIGURE 10. Classification Results of the Enhanced HSI by DCP. The (a), (b), (c) and (d) are the classification results of ROI1 using SAM, SVM, DBN and CNN with 10% training data respectively. The (e), (f), (g) and (h) are the classification results of ROI2 using SAM, SVM, DBN CNN with 10% training data respectively. The (i), (j), (k) and (l) are the classification results of ROI1 using SAM, SVM, DBN and CNN with 20% training data respectively. The (m), (n), (o) and (p) are the classification results of ROI2 using SAM, SVM, DBN and CNN with 20% training data respectively.
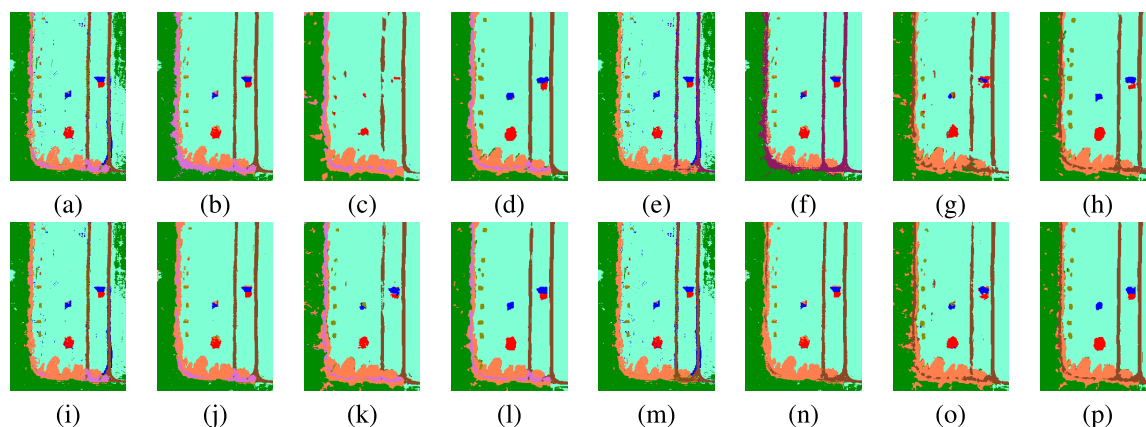
From Table 3 and Fig. 9 to 12, it is obvious that the enhancement effect by DCP method is not ideal for the HYDICE HSI and the corresponding classification results are even worse than those of the original image without enhancement, because DCP is designed only for the RGB images rather than HSIs.

FIGURE 11. Classification Results of the Enhanced HSI by DSR on Spatial Dimension. The (a), (b), (c) and (d) are the classification results of ROI1 using SAM, SVM, DBN and CNN with 10% training data respectively. The (e), (f), (g) and (h) are the classification results of ROI2 using SAM, SVM, DBN CNN with 10% training data respectively. The (i), (j), (k) and (l) are the classification results of ROI1 using SAM, SVM, DBN and CNN with 20% training data respectively. The (m), (n), (o) and (p) are the classification results of ROI2 using SAM, SVM, DBN and CNN with 20% training data respectively.
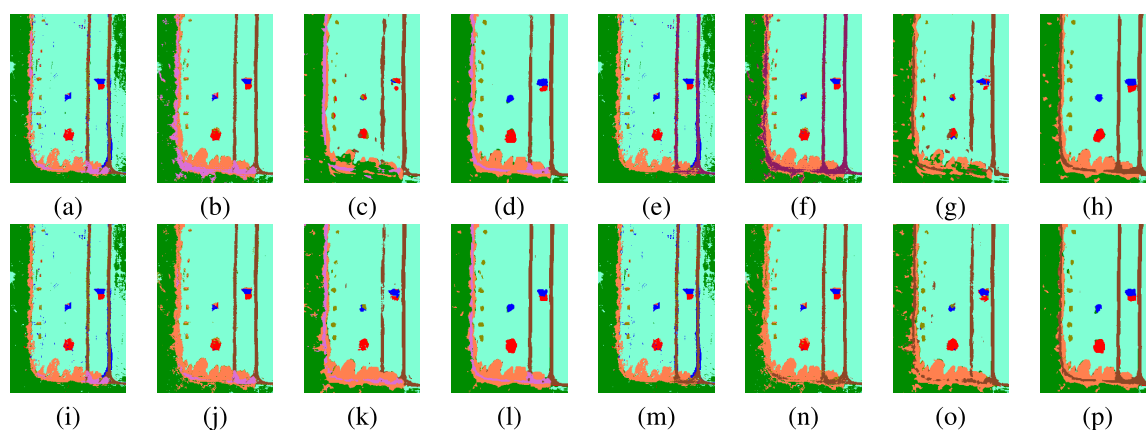
FIGURE 12. Classification Results of the Enhanced HSI by DSR on Spectral Dimension. The (a), (b), (c) and (d) are the classification results of ROI1 using SAM, SVM, DBN and CNN with 10% training data respectively. The (e), (f), (g) and (h) are the classification results of ROI2 using SAM, SVM, DBN CNN with 10% training data respectively. The (i), (j), (k) and (l) are the classification results of ROI1 using SAM, SVM, DBN and CNN with 20% training data respectively. The (m), (n), (o) and (p) are the classification results of ROI2 using SAM, SVM, DBN and CNN with 20% training data respectively.

It can also be seen that the deep-learning based methods, DBN and 2D-CNN, notably the latter, have the advantage in HSI classification comparing to the conventional methods, SAM and SVM.

According to Fig. 9, 11 and 12, especially from Table 3, it can be known that DSR can help to improve the classification and the enhancement in the spectral dimension has more promising prospective than in the spatial dimension in most cases.

For different percentage of the training data, generally, more training data is, better classification result will be, which can be supported by the OA values in Table 3. In particular, when the training data are small, for example, 10%, the classification with ROI1 (including "road under shadow") is superior to that with ROI2, which can be seen from the italic bold OA values in Table 3. It means that the proposed method combining DSR and 2D-CNN has potential

capability in the HSI information exploration of the shadow areas containing different targets with small samples.

V. CONCLUSION

The enhancement and the classification of the shadow areas in HSIs are difficult due to low reflection and small samples. In this paper, an improved method with DSR and 2D-CNN is proposed to process shadow areas in HSIs. Firstly, DSR is used to enhance the shadow areas on the spatial and the spectral dimensions respectively. Then the enhanced shadow areas can be fused with the original HSI. Finally, the processed image could be classified by 2D-CNN. The performance of the proposed method are compared with the considered methods on a real-word HYDICE HSI. The experimental results show DSR outperforms DCP in shadow areas enhancement of HSIs and 2D-CNN has better classification ability than other considered methods. Therefore, the proposed method

has promising prospective in the information exploration of the shadow areas with small samples and different targets.

Although 2D-CNN is convenient to process DSR enhanced data, the 3D tensor characteristic of HSIs has not been taken into account. So, the results in the paper encourage us to further explore the 3D DSR enhancement method so that 3D-CNN can be used and the spatial-spectral features of HSIs can also be fully utilized.

REFERENCES

[1] J. Ren, X. Jia, W. Liao, and L. Gao, "Guest editorial: Hyperspectral imaging and applications," *IET Image Process.*, vol. 13, no. 2, pp. 233–234, Feb. 2019.

[2] F. D. van der Meer, H. M. A. van der Werff, F. J. A. van Ruitenbeek, C. A. Hecker, W. H. Bakker, M. F. Noomen, M. van der Meijde, E. J. M. Carranza, J. B. de Smeth, and T. Woldai, "Multi- and hyperspectral geologic remote sensing: A review," *Int. J. Appl. Earth Observ. Geoinf.*, vol. 14, pp. 112–128, Feb. 2012.

[3] C. Gong, L. Jia-Xuan, W. Chao-Peng, H. Zhen-Guang, and N. Qing-kun, "Study on hyperspectral quantitative inversion of ionic rare earth ores," *Spectroscopys Spectral Anal.*, vol. 39, no. 5, pp. 1571–1578, May 2019.

[4] N. Kayet, K. Pathak, A. Chakrabarty, S. Kumar, V. M. Chowdary, C. P. Singh, S. Sahoo, and S. Basumatary, "Assessment of foliar dust using hyperion and landsat satellite imagery for mine environmental monitoring in an open cast iron ore mining areas," *J. Cleaner Prod.*, vol. 218, pp. 993–1006, May 2019.

[5] X. Tong, L. Duan, T. Liu, and V. P. Singh, "Combined use of *in situ* hyperspectral vegetation indices for estimating pasture biomass at peak productive period for harvest decision," *Precis. Agricult.*, vol. 20, no. 3, pp. 477–495, Jun. 2019.

[6] X. Qiao, D. Yuan, and H. Li, "Urban shadow detection and classification using hyperspectral image," *J. Indian Soc. Remote Sens.*, vol. 45, no. 6, pp. 945–952, 2017.

[7] W. Zhai, W. Zhang, B. Chen, and C. Cheng, "Hyperspectral analysis of objects under shadow conditions based on field reflectance measurements," *Appl. Opt.*, vol. 58, no. 17, pp. 4797–4805, 2019.

[8] L. Windrim, R. Ramakrishnan, A. Melkumyan, and R. J. Murphy, "A physics-based deep learning approach to shadow invariant representations of hyperspectral images," *IEEE Trans. Image Process.*, vol. 27, no. 2, pp. 665–677, Feb. 2018.

[9] L. He, J. Li, C. Liu, and S. Li, "Recent advances on spectral–spatial hyperspectral image classification: An overview and new guidelines," *IEEE Trans. Geosci. Remote Sens.*, vol. 56, no. 3, pp. 1579–1597, Mar. 2017.

[10] L. Xie, G. Li, M. Xiao, L. Peng, and Q. Chen, "Hyperspectral image classification using discrete space model and support vector machines," *IEEE Geosci. Remote Sens. Lett.*, vol. 14, no. 3, pp. 374–378, Mar. 2017.

[11] Y. Liu, S. Lu, X. Lu, Z. Wang, C. Chen, and H. He, "Classification of urban hyperspectral remote sensing imagery based on optimized spectral angle mapping," *J. Indian Soc. Remote Sens.*, vol. 47, no. 2, pp. 289–294, Feb. 2019.

[12] Y. Zhao, Y. Yuan, and Q. Wang, "Fast spectral clustering for unsupervised hyperspectral image classification," *Remote Sens.*, vol. 11, no. 4, p. 399, Feb. 2019.

[13] Y. Chen, X. Zhao, and X. Jia, "Spectral-spatial classification of hyperspectral data based on deep belief network," *IEEE J. Sel. Topics Appl. Earth Observ. Remote Sens.*, vol. 8, no. 6, pp. 2381–2392, Jun. 2015.

[14] Y. Li, H. Zhang, and Q. Shen, "Spectral–spatial classification of hyperspectral imagery with 3D convolutional neural network," *Remote Sens.*, vol. 9, no. 1, p. 67, 2017.

[15] A. Sellami, M. Farah, I. R. Farah, and B. Solaiman, "Hyperspectral imagery classification based on semi-supervised 3-D deep neural network and adaptive band selection," *Expert Syst. Appl.*, vol. 129, pp. 246–259, Sep. 2019.

[16] K. He, J. Sun, and X. Tang, "Single image haze removal using dark channel prior," *IEEE Trans. Pattern Anal. Mach. Intell.*, vol. 33, no. 12, pp. 2341–2353, Dec. 2011.

[17] E. H. Land and J. J. McCann, "Lightness and Retinex theory," *J. Opt. Soc. Amer.*, vol. 61, no. 1, pp. 1–11, 1971.

[18] R. Benzi, A. Sutera, and A. Vulpiani, "The mechanism of stochastic resonance," *J. Phys. A, Math. Gen.*, vol. 14, no. 11, pp. L453–L457, 1981.

[19] N. Gupta and R. K. Jha, "Enhancement of dark images using dynamic stochastic resonance with anisotropic diffusion," *J. Electron. Imag.*, vol. 25, no. 2, 2016, Art. no. 023017.

[20] N. Gillard, É. Belin, and F. Chapeau-Blondeau, "Stochastic resonance with unital quantum noise," *Fluctuation Noise Lett.*, vol. 18, no. 3, Mar. 2019, Art. no. 1950015.

[21] H. Bi, Y. Lei, and Y. Han, "Stochastic resonance across bifurcations in an asymmetric system," *Phys. A, Stat. Mech. Appl.*, vol. 525, pp. 1296–1312, Jul. 2019.

[22] R. Chouhan, R. K. Jha, and P. K. Biswas, "Enhancement of dark and low-contrast images using dynamic stochastic resonance," *IET Image Process.*, vol. 7, no. 2, pp. 174–184, Mar. 2013.

[23] Y. LeCun, B. Boser, J. S. Denker, D. Henderson, R. E. Howard, W. Hubbard, and L. D. Jackel, "Backpropagation applied to handwritten zip code recognition," *Neural Comput.*, vol. 1, no. 4, pp. 541–551, 1989.

[24] A. Krizhevsky, I. Sutskever, and G. E. Hinton, "ImageNet classification with deep convolutional neural networks," *Commun. ACM*, vol. 60, no. 6, pp. 84–90, May 2017.

[25] N. He, Mercedes E. Paoletti, J. M. Haut, L. Fang, S. Li, A. Plaza, and J. Plaza, "Feature extraction with multiscale covariance maps for hyperspectral image classification," *IEEE Trans. Geosci. Remote Sens.*, vol. 57, no. 2, pp. 755–769, Feb. 2019.

[26] Q. Zhang, J. Chang, G. Meng, S. Xu, S. Xiang, and C. Pan, "Learning graph structure via graph convolutional networks," *Pattern Recognit.*, vol. 95, pp. 308–318, Nov. 2019.

[27] Z. Zuo, B. Shuai, G. Wang, X. Liu, X. Wang, B. Wang, and Y. Chen, "Learning contextual dependence with convolutional hierarchical recurrent neural networks," *IEEE Trans. Image Process.*, vol. 25, no. 7, pp. 2983–2996, Jul. 2016.

[28] Y.-L. He, X.-L. Zhang, W. Ao, and J. Z. Huang, "Determining the optimal temperature parameter for Softmax function in reinforcement learning," *Appl. Soft Comput.*, vol. 70, pp. 80–85, Sep. 2018.

[29] S. Afyouni, S. M. Smith, and T. E. Nichols, "Effective degrees of freedom of the Pearson's correlation coefficient under autocorrelation," *NeuroImage*, vol. 199, pp. 609–625, Oct. 2019.

[30] A. Genovese, V. Piuri, K. N. Plataniotis, and F. Scotti, "PalmNet: Gabor-PCA convolutional networks for touchless palmprint recognition," *IEEE Trans. Inf. Forensics Security*, vol. 14, no. 12, pp. 3160–3174, Dec. 2019.

[31] X. Liu, S. Bourennane, and C. Fossati, "Denoising of hyperspectral images using the PARAFAC model and statistical performance analysis," *IEEE Trans. Geosci. Remote Sens.*, vol. 50, no. 10, pp. 3717–3724, Oct. 2012.

[32] X. Liu, Q. Sun, Y. Meng, M. Fu, and S. Bourennane, "Hyperspectral image classification based on parameter-optimized 3D-CNNs combined with transfer learning and virtual samples," *Remote Sens.*, vol. 10, no. 9, p. 1425, Sep. 2018.
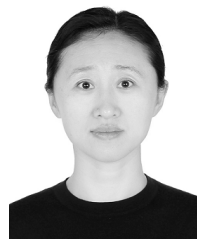
XUEFENG LIU received the B.S. degree in electronics and information system and the M.S. degree in circuits and systems from Shandong University, Shandong, China, in 1999 and 2002, respectively, and the Ph.D. degree in optics photonics and image processing from École Centrale Marseille, Marseille, France, in 2012, where she did postdoctoral research, in 2018.

She is currently an Associate Professor with the Qingdao University of Science and Technology. She has published more than 30-related academic articles indexed by SCI and EI, in relevant journals or international conferences. Her current research includes hyperspectral image processing, signal processing, and ocean information processing.

HAO WANG was born in Taian, China, in 1996. He received the B.E. degree in electronic information engineering and technology from the Qingdao University of Science and Technology, Qingdao, China, in 2018, where he is currently pursuing the M.S. degree in control science and engineering.

His current research interests include image processing, hyperspectral image processing, and hyperspectral image target detection and classification.

YUE MENG was born in Dezhou, China, in 1993. She received the B.E. degree in automation from Suihua University, Suihua, China, in 2017. She is currently pursuing the M.E. degree in control engineering with the Qingdao University of Science and Technology, Qingdao, China.

Her current research interests include image processing, hyperspectral image processing, and hyperspectral image target detection and classification.

MIN FU received the B.S. degree in electronics and information system and the M.E. degree in signal and information processing from the Ocean University of China, Qingdao, China, in 1998 and 2004, respectively, and the D.E. degree in microelectronics and solid state electronics from the Dalian University of Technology, Dalian, China, in 2012.

He is currently an Associate Professor with the Ocean University of China. He has published more than 20-related academic articles in relevant journals or international conferences indexed by SCI and EI. His current research interests include signal processing, image processing, and communication under water.

● ● ●